Chapter 4

Experimental Apparatus

All experimental results presented in this thesis are obtained with ion and electron time of flight (TOF) spectroscopy. These techniques combine a rather simple mechanical setup with low cost and simplicity of operation. It is able to provide complete mass or photoelectron spectra for each ionisation event without the necessity for scanning through voltage settings to select certain intervals of masses or kinetic energies. At the same time, fast electronic data acquisition schemes allow one to increase the signal to noise ratio in a short analysis time by instantaneous averaging of individual spectra obtained in every event of ionisation, even in the case of high repetition rates, typically $1\,\mathrm{kHz}$. Another advantage of TOF spectrometry is wide detection range of masses or kinetic energies. This makes it well suited for gas phase investigations of large molecules and clusters [PMi90].

This chapter begins with a description of the vacuum chamber and the molecular beam-source. After that, the general principles of TOF spectroscopy as well as the spectrometer and the detection schemes used during this work are presented.

4.1 Vacuum Chamber

The vacuum chamber is shown in Fig. 4.1. It consists of three separately pumped parts: a laser ionisation chamber, an electron TOF chamber, and an ion TOF chamber. The laser ionisation chamber contains the molecular beam source and a cold trap. A laser beam comes through the entrance window (diameter $D = 10\,\mathrm{mm}$ and thickness $h = 250\,\mu\mathrm{m}$) and crosses the molecular beam and the spectrometer axis perpendicularly. The vacuum in this ionisation chamber is maintained by a large turbo-molecular pump (TMU 1001P, Pfeiffer Vacuum Tech-

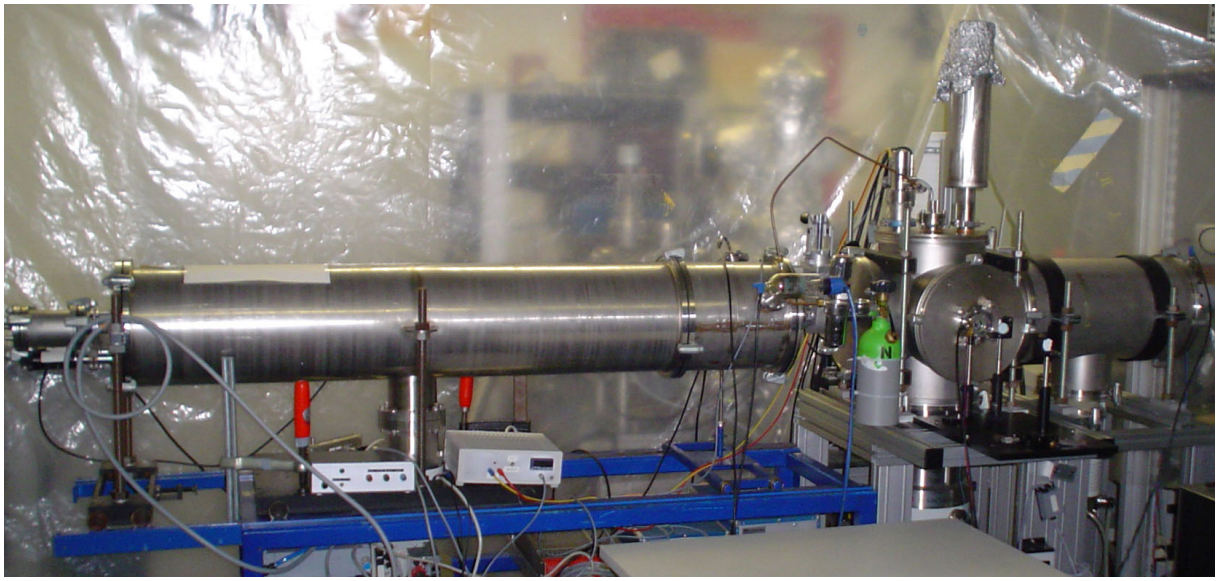

Figure 4.1: Photograph of the vacuum apparatus consisting of ion TOF chamber, laser ionisation source chamber, and electron TOF chamber (from left to right).

nology). The ion TOF chamber is evacuated by a smaller turbo-molecular pump (TMU 260, Pfeiffer Vacuum Technology). The third and smallest turbo-molecular pump (TPH 180H, Pfeiffer Vacuum Technology) is used to keep vacuum inside the electron TOF chamber.

A pair of Bayard-Alpert type ionisation tubulated gauges (model 274003, Granville-Phillips) controls the pressure inside the vacuum chamber. By using three turbomolecular pumps the background pressure is maintained between 1.3×10^{-7} mbar and 3.3×10^{-7} mbar. One needs around 24 hours to reach such pressure after the chamber has been vented. Longer times are required for the reduction of the water residual gas in the chamber. This can be very important for experiments using high laser intensities. The cold trap filled with liquid nitrogen allows one to further decrease the pressure approximately by one order of magnitude. The presence of the low density effusive molecular beam in the ionisation chamber does not influence the background pressure. For purposes of calibration and alignment a constant flow of Xenon is supplied in most experiments raising the pressure in the ionisation chamber to a range between 0.7×10^{-6} mbar and 1.3×10^{-6} mbar (depending on the used laser intensity).

4.2 Molecular Beam Source

For gas-phase investigations of molecules and clusters one needs to have suitable beam

sources. Different methods of beam generation can be applied. Most important and commonly used among them are: effusive beam source [Ste86, BGM93] and adiabatic beam expansion in a jet nozzle [KGr51, AFe65]. The first method involves a gas effusion from an oven or a source cavity through an aperture into a high vacuum chamber. The gas in the oven or the source cavity is at a density sufficiently low so that molecules undergo no collisions when passing through the aperture. Any effusive beam has to satisfy the following conditions: i) collisions between particle inside the beam are negligible and ii) mean free path Λ is much larger than diameter of the source aperture d.

The main idea of the second method is a supersonic jet expansion from a high pressure gas source into a chamber maintained at high vacuum by continuous pumping. In this case the thermal energy of the gas transforms directly to kinetic energy of molecular motion predominantly ordered in the direction of a supersonic flow. As a result, a molecular beam with narrow velocity and angular distributions as well as a high particle density is formed.

In many cases, mass spectroscopic studies with intense laser fields do not require large particle densities in a molecular beam and effusive beam sources are more preferable than jet nozzles. In the present studies an effusive molecular beam is produced by the evaporation of sample powders in a resistively heated oven. A microprocessor controller (JUMO iTRON 32, JUMO GmbH) is used to stabilise the oven temperature with an accuracy better than 0.2%. In the case of experiments with C_{60} fullerenes the temperature range is $500 \pm 10\,^{\circ}$C, except for some experiments with photoelectrons done at $640\,^{\circ}$C. Experiments with model peptides are performed at oven temperatures between $70\,^{\circ}$C and $130\,^{\circ}$C. The temperature values used will be specified when the corresponding data are presented.

A photograph of the oven is shown in Fig. 4.2. The molecular beam is formed by expansion of the heated gas into free space through the source aperture with diameter $d_A = 1\,$mm. A diaphragm with diameter $d_D = 1\,$mm is placed to collimate the molecular beam in the interaction region. The distances between the source aperture and the diaphragm and between the source aperture and the interaction region are $L_D = 1\,$cm and $L_I = 5\,$cm, respectively. A pure geometrical approximation of the molecular beam diameter D_m at the interaction region assuming the absence of the collisions between particles and the diaphragms can be done with the following formula

$$D_m = \frac{L_I}{L_D} d_D \quad . \tag{4.1}$$

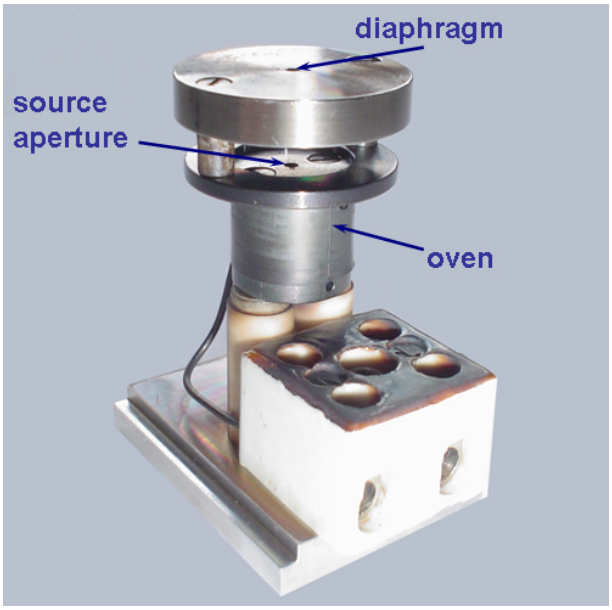

Figure 4.2: Photograph of the oven.

For the data given above the molecular beam diameter is $D_m = 5\,\text{mm}$.

To check the validity of an effusive beam assumption ($\Lambda \gg d_A$) one has to calculate the C_{60} mean free path Λ which depends on the collisional (geometrical) cross-section σ_g and the particle density n

$$\Lambda = \frac{1}{\sqrt{2}\sigma_g n} \quad . \tag{4.2}$$

Assuming ideal gas conditions and using $n = 4.1 \times 10^{19}\,\text{m}^{-3}$ at the temperature of $500\,^\circ\text{C}$ [JKa00] and $\sigma_g = 336\,\text{Å}^2$ [DDE96] the mean free path for C_{60} is $\Lambda = 5.2\,\text{mm}$. It is larger (but not considerably larger) than the source aperture diameter. Therefore, under current experimental conditions the assumption of an effusive beam flow is still possible.

The flow dN/dt of the particles emerging from the oven into a solid angle $d\Omega$ with velocities lying within dv is given according to [Est46] by

$$\frac{dN}{dt} d\Omega dv = \frac{P}{16kT} f(v) v \cos(\theta) d_A^2 d\Omega dv \quad , \tag{4.3}$$

where v is the velocity of an emerging particle, $f(v)$ is the velocity distribution in the source, P is the gas pressure in the source, T is the gas temperature, θ is the angle with respect to the source aperture normal, and k is the Boltzmann constant. Integration over all possible velocities gives the total flow $I(\theta)$

$$I(\theta) = \frac{P\langle v \rangle d_A^2}{16kT} \cos(\theta) \quad , \tag{4.4}$$

where $\langle v \rangle$ is the average velocity in the source gas. The angular distribution of the emerged particles follows a cosine law with a maximum in forward direction ($\theta = 0$). The particle density in the interaction region n_L can be calculated using the formula [Ram90]

$$n_L = \frac{1}{12\sqrt{\pi}} \left(\frac{d_A}{L_I}\right)^2 n \quad , \tag{4.5}$$

where n is the particle density in the source.

The particles velocities v in a molecular beam are described by the Maxwell-Boltzmann distribution

$$f(v) = 4\pi \sqrt{\left(\frac{m}{2\pi kT}\right)^3} v^2 e^{-\frac{mv^2}{2kT}} \quad , \tag{4.6}$$

where m is the mass of a particle. The most probable velocity v_p, the average velocity $\langle v \rangle$, and the root mean square velocity v_{rms} of the Maxwell-Boltzmann distribution are

$$v_p = \sqrt{\frac{2kT}{m}} \quad , \tag{4.7}$$

$$\langle v \rangle = \sqrt{\frac{8kT}{\pi m}} \quad , \tag{4.8}$$

and

$$v_{rms} = \sqrt{\frac{3kT}{m}} \quad . \tag{4.9}$$

According to Eq. (4.7)-(4.9) v_p, $\langle v \rangle$, and v_{rms} for C_{60} at the temperature of $500\,^{\circ}$C are $133.6\,$m/s, $150.8\,$m/s, and $163.7\,$m/s, respectively. On a typical time scale of the pump-probe experiments ($500\,$fs) such velocities correspond to a C_{60} drift of about $0.75\,$Å only. Thus, the C_{60} can be considered space fixed during the interaction time with the laser.

4.3 Time of Flight Mass Spectrometry

Time of flight (TOF) mass spectrometry is based on the measurement of the time that it takes for an ion to reach a detector after an ionisation event while travelling over a known distance [Gui95, Mam01, GVa03]. In the most simple arrangement the ions created are accelerated by an electric filed over a finite distance (acceleration region) to a well defined kinetic energies. They then fly through a field free (drift) region and, finally, are registered by a detector. The arrival time t at the detector for a fixed kinetic energy of all ions starting from

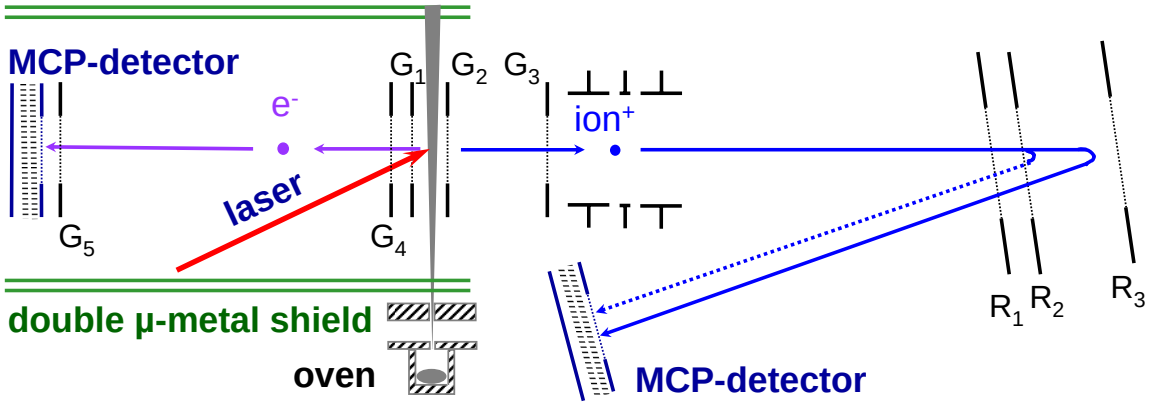

Figure 4.3: Scheme of reflectron TOF mass spectrometer (right part) and photoelectron spectrometer (left part). For the distances and applied voltages see Table 4.1 and Table 4.2.

the same point at the same time (so-called "time of flight") depends on their mass m to charge q ratio

$$t \propto \sqrt{\frac{m}{q}} \quad . \tag{4.10}$$

Thus, by measuring this time t, the mass to charge ratio m/q of the ion can be determined.

The resolution R of a mass spectrometer is defined as the ability to distinguish two ions of different masses

$$R = \frac{m}{\Delta m} \quad , \tag{4.11}$$

where Δm is the mass difference of the two ions. Since $m \propto t^2$ and $\Delta m/\Delta t \propto 2t$, the resolution R can by written as

$$R = \frac{t}{2\Delta t} \quad , \tag{4.12}$$

where Δt is usually the full width at half maximum (FWHM) of a mass peak. It is clear that the mass resolution R can be improved by increasing t (low acceleration potential or/and long drift length) or narrowing the peak width Δt.

A schematic picture of the reflectron TOF mass spectrometer employed in the present work is shown in the right part of Fig. 4.3. Distances between grids and potentials applied to them are illustrated in Table 4.1. Ions are originated inside the dual stage space focusing system of three electrodes (G_1, G_2, and G_3) forming two electric fields. The magnitudes of both fields are

Table 4.1: Voltage settings used in this work and distances between grids of the reflectron TOF mass spectrometer.

Region	Voltage, V	Distance, mm
G_1 - G_2	2470 - 2076	20
G_2 - G_3	2076 - GND	60
G_3 - R_1	GND - GND	1530
R_1 - R_2	GND - 1670	26
R_2 - R_3	1670 - 2800	234
R_1 - MCP	GND - GND	1086

chosen to meet well known Wiley-McLaren spatial focusing conditions [WMc55, SRe01]. The extraction electric field with strength of $1.97 \times 10^4\,\mathrm{V/m}$ pushes the ions out of the ionisation region into the acceleration region. Here the uniform electric field with strength $3.46 \times 10^4\,\mathrm{V/m}$ accelerates the ions into the first field free drift region. The length of this region is $1.53\,\mathrm{m}$. The drift through this field free region allows the ions to be separated depending on their mass to charge ratios. Then the ions reach the reflectron [MKS73]. This is a device consisting of three electrodes (R_1, R_2, and R_3) which produce two electric fields: decelerating (for incoming ions)/accelerating (for outgoing ions) and reflecting. In order to improve the homogeneity of the electric field in the reflectron a number of equally spaced ring electrodes is placed between the end electrodes, connected by a chain of resistors. The first electrode is grounded, while the second one is at a voltage which creates the decelerating or retarding electric field slowing the ions to approximately $75\,\%$ of their velocity. The electric field between the second and the third electrodes reflects the electrons back at an angle of 2° with respect to the TOF axis. Finally, the same electric field that was used for the deceleration now accelerates the ions back out of the reflectron in the direction of the detector so that they leave with the same velocity they have entered it. The ions with higher kinetic energy penetrate the reflecting field further than the ions with lower kinetic energy, hence, the faster ions have to travel larger distances inside the reflectron and spend more time there. By choosing the appropriate geometry and

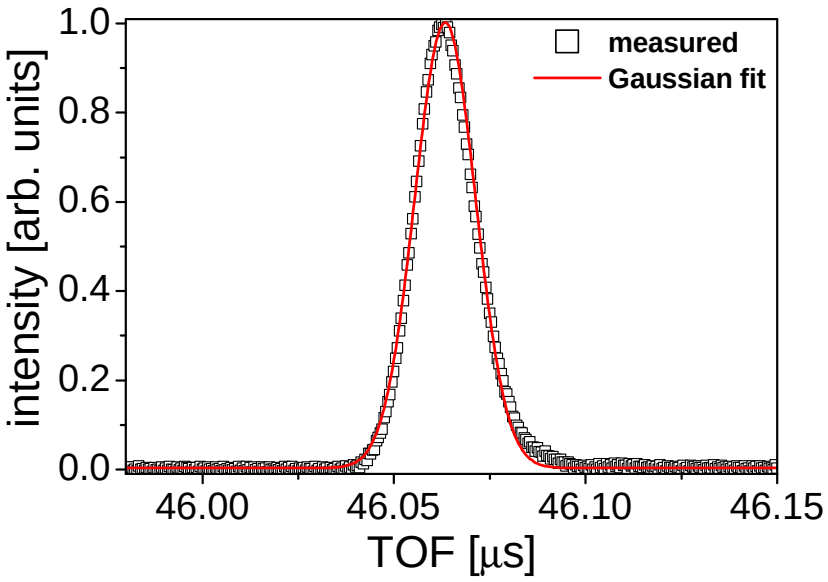

Figure 4.4: Experimentally measured shape and Gaussian fit of Xenon peak with mass 129 u. The width of the peak (FWHM) is 18.7 ns or 0.1 u.

voltages the shortest flight time of the high energy ions in the drift region is compensated by their longer residence time within the reflectron. After the reflection the ions drift through a second field free region for further mass separation and, finally, reach a detector. The total distance between the interaction region and the detector is ≈ 3.2 m. This length together with the actual voltage settings give flight times in the range between $\approx 5\,\mu$s (for H^+) and $\approx 160\,\mu$s (for C_{60}^+). Assuming that the average thermal velocity of molecules in the C_{60} beam is 150 m/s, the corresponding perpendicular drift during the flight time on the way to the detector is 24 mm. Such drift is not much smaller than the detector size (see Sec. 4.5). Therefore, some loss of resolution for heaviest ions due to missing the detector is possible.

A peak shape of Xenon ion with mass 129 u as well as a Gaussian fit is presented in Fig. 4.4. The width of the peak (FWHM) is 18.7 ns or 0.1 u. This corresponds to a resolution of $\approx 1.2 \times 10^3$. The peak shape is slightly asymmetric with respect to the fit. This is a result of not a full spatial focusing, where the ions produced far from the centre of the interaction region have larger flight times than the ions formed in the mean part of the interaction region.

Peak broadening and, hence, resolution losses are caused by a spread in ions arrival times. The spread arises due to three major reasons: i) the distribution of initial kinetic energies (velocities) of ions, ii) the distribution of positions where, and iii) the distribution of times when ions are formed in the interaction region prior the acceleration. Of course, there are several minor additional factors for resolution losses such as space charge effects, ions collisions, and different kinds of instrumental effects. These factors play, however, a minor role and will not be discussed here.

The simplest peak broadening reason arises from ions formed at slightly different times. Such ions, even when produced at the same position with equal kinetic energies, will reach the detector with a spread of arrival times. Therefore, the resolution will be reduced. This temporal distribution can arise, for example, from the finite pulse duration of the laser used for the ionisation. In the case of Xenon ion shown in Fig. 4.4 this peak broadening factor along even on a typical time scale of the pump-probe experiments ($\approx 500\,\mathrm{fs}$) corresponds to the resolution of $\approx 4.6 \times 10^7$. Therefore, this effect is completely irrelevant for the experiments presented here. Nevertheless, the resolution can be further improved by the enlarging of the flight time using either a longer field free region or a lower acceleration potential. A second possibility to improve the resolution is the application of more complicated and sophisticated techniques such as "time-lag-focussing" [WMc55], "impulse-field-focussing" [BMT81], "rapid field reversal" [MHo84], or the combination of TOF mass spectrometry with momentum focusing by a magnetic sector [Pos71].

The next peak broadening factor comes from the ions spatial distribution, when ions are produced at different space points, for example, due to a finite size of the interaction region of an ionising laser. This distribution creates a spread of ion kinetic energies after acceleration because ions formed far from the detector obtain larger final kinetic energies by travelling longer distances through the electric field than ions formed closer to the detector. For Xenon ion shown in Fig. 4.4 assuming the waist of the interaction region is $72.3\,\mu$m (see Sec. 6.2) only this peak broadening factor leads to the resolution of $\approx 1.1 \times 10^4$. Since ions formed close to the detector have shorter flight distances than ions formed far from the detector, it is possible by adjusting the electric field strength to find conditions of space focusing [WMc55, SRe01], when this spatial distribution and resulting spread of kinetic energies after acceleration compensate each other. As a result, ions of any given mass will arrive to the space focus plane at the same

time.

The last peak broadening factor is due to the initial velocities and, hence, kinetic energies distribution, when ions with different initial velocities arrive to the detector at different times. There are ions which initially move towards the field free region as well as ions which move in the opposite direction. The latter have to be decelerated first, then accelerated back and will pass through their initial positions after the so-called "turn-around time". Two ions starting with the same velocity but in opposite initial directions, thus, obtain the same final velocity. Their arrival times at the detector are separated by the turn-around time. This can be used to extract information about the initial kinetic energies of ions. But in most cases this effect is undesirable and it leads to the lost of a resolution. For example, for Xenon ion shown in Fig. 4.4 assuming the initial velocity of $240\,\mathrm{m/s}$ the resolution is $\approx 0.7 \times 10^3$ only. Hence, this is the most significant factor of resolution loses in the present experimental setup. The simplest way to improve the resolution is the operation with longer field free region. But the best solution for correcting the initial kinetic energy spread is to use a reflectron. Utilisation of the reflectron allowed to improve the resolution for Xenon ion up to $\approx 1.2 \times 10^3$.

4.4 Photoelectron Spectroscopy

The scheme of the photoelectron spectrometer is presented in the left part of Fig. 4.3. Distances between grids and potentials applied to them are summarised in Table 4.2. To obtain the highest possible temporal resolution and to prevent the corruption of the photoelectrons original kinetic energy distribution no extra electric field is applied to the grids.

It is important to shield the electrons flight region from the influence of the earth magnetic field or magnetic fields induced by currents. A double μ-metal shield is used for that. This shield consists of two concentric tubes made from nickel-iron alloy with diameters $130\,\mathrm{mm}$ and $110\,\mathrm{mm}$, respectively. A copper tube with an inner diameter of $48\,\mathrm{mm}$ and a length of $450\,\mathrm{mm}$ is put inside. The inner surface of this copper tube is coated with graphite to avoid charging effects. The double μ-metal shield system provides the magnetic field shielding around four orders of magnitude [Boy05].

Since the photoelectrons are emitted into the full solid angle 4π and no electric extraction field is applied, only a very small fraction of the photoelectron reaches the detector. This

Table 4.2: Voltage settings used in this work and distances between grids of the photoelectron spectrometer.

Region	Voltage, V	Distance, mm
G_2 - G_1	GND - GND	20
G_1 - G_4	GND - GND	10
G_4 - G_5	GND - GND	~ 445
G_5 - MCP	GND - GND	10

fraction can be estimated from the inner diameter of the internal flight tube (48 mm) and the distance between the interaction region and the photoelectron detector (475 mm). For the present design the acceptance angle is $\sim 2.9^\circ$ corresponding to a fraction of the photoelectrons reaching the detector of $\sim 0.7\%$.

Unfortunately, the simultaneous detection of electrons and ions can not be achieved with the present experimental apparatus. But it is possible to switch between photoelectron and mass spectrometer operation very fast without breaking the vacuum and carry out the measurements under almost identical conditions.

4.5 Ion and Electron Detection

Ions and photoelectrons are registered using a microchannel plate (MCP) detector. Such detectors are widely used in a variety of applications for detecting and imaging of ions [KZT05], electrons [KWK86], protons [FSH96], ultraviolet [FHD83] and X-ray photons [Shi97] providing high spatial and temporal resolution, high gain, low background signal rates, and stability against the magnetic field influence.

The individual MCP used in this work (MCP-56-15, TOPAG GmbH) represents a lead glass plate of 0.8 mm thickness and round shape with a diameter of 50 mm. The front and back surfaces of the MCP is coated with metal. It has a pore structure and contain in one square centimeter up to one million of separate channels of $15\,\mu$m nominal diameter coated with semiconducting lead oxide (PbO). All channels have 10° tilt with respect to the MCP

surface normal, so-called "channel bias angle". In the present work a pair of MCPs is used in chevron-type (or V-stack) configuration for the detection both ions and photoelectrons. In this configuration the tilt of the channels in the two plates with respect to the spectrometer axis is opposite. The channel tilt obviates the passing of incident particles through the MCP without interaction. Since particles falling on the MCP between the channels can not be detected, the MCP detection sensitivity depends on the open area ratio(OAR). It is a ratio of the MCP open area (integrated pore area) to the MCP total effective area. The OAR can be calculated as

$$OAR = \frac{\pi}{2}\left(\frac{d}{P}\right)^2 \quad , \tag{4.13}$$

where P is a period of the pore structure. For MCP-56-15 OAR is 63%. According the specification typical operation voltage at 10^4 gain is $1100\,\mathrm{V}$ per plate.

The detection mechanism of incident particles by the MCP has been studied in detail [Wiz79]. An incident particle hits a channel of the MCP detector producing secondary electrons by the emission from the channel wall. Each secondary electron is accelerated further into the cannel by an applied electric field and strikes the channel wall generating more and more secondary electrons and, finally, forming a cloud of cascade electrons. This electron cloud hits the anode and it is detected by the electronics.

Fig. 4.5a illustrates the ion detection scheme used in this work. Before entering the MCP ions can be further accelerated by the acceleration voltage U_{AC} applied between the grounded grid and the MCP front surface. The power supply scheme is realised in such way that it allows one to hold the bias voltage U_{MCP} between the front and back surfaces of the MCPs constant while varying U_{AC} in a wide range. In the present work U_{AC} and U_{MCP} are set to $-2.0\,\mathrm{kV}$ and $-2.2\,\mathrm{kV}$, respectively.

Detection efficiency is one of the most important characteristics of MCPs. The MCP detection efficiency for different kinds of incident particles, their masses and kinetic energies has been investigated by many groups [GSe00, YNK01, KZT05]. The highest detection efficiency is observed for electrons, the lowest – for UV photons and X-rays [Wiz79]. For positive ions the detection efficiency varies between $5\,\%$ and $85\,\%$ [Wiz79] depending on their composition and velocities [GSe00]. Two different physical mechanisms determine the detection efficiency for positive ions: kinetic and potential emission of secondary electrons [Kre68]. The kinetic emission is induced by direct collision of the ions with an MCP material and it depends on

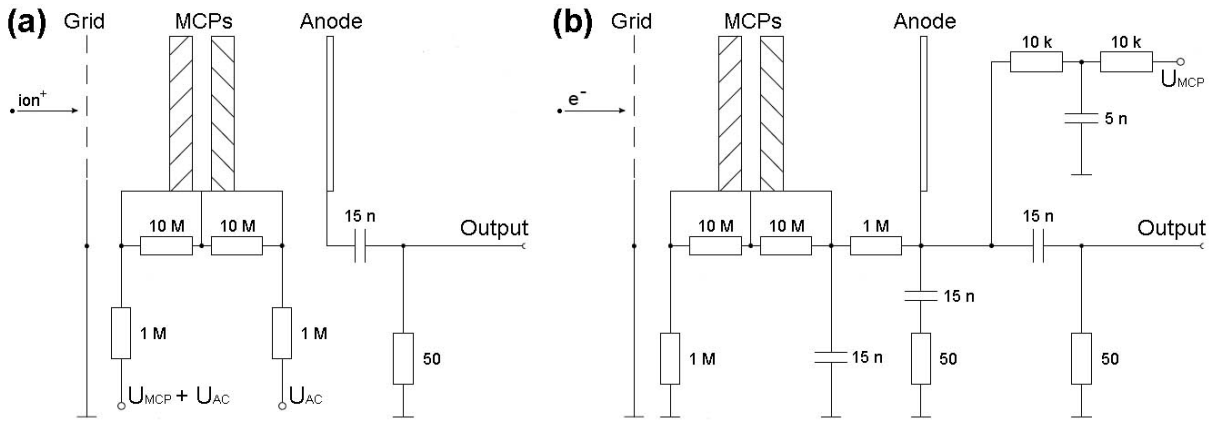

Figure 4.5: The schemes used for the detection of: a)ions and b)electrons.

ions velocities and masses. The yield of secondary electrons caused by this process rises as a function of ion impact energies. If the work function of the MCP material is less than one half of the ion ionisation potential, the potential emission can play an essential role [GSe00]. This process is independent of ion impact energies but it depends on an ion internal energy. Therefore, it is sensitive to the charge of ions. Usually, the potential emission dominates over the kinetic emission at low ion impact energies.

The detection efficiency for C_{60} fullerenes is well known and described as follows [ITM99]

$$F = 1 - e^{-\frac{1.48E+2.18E^2}{100}} \quad , \tag{4.14}$$

where F is the detection efficiency and E [keV] is the ion impact energy. For the experiments involving the comparison of the absolute abundances for the different charge states of C_{60} (for example, intensity dependent studies) measured ion yields are rescaled with the detection efficiency described by Eq. (4.14). In the present work the ion impact energies are 6.47, 12.95, and 19.42 keV for single, double, and triple charged C_{60} ions at $U_{AC} = -2.0$ kV (taking into account U_{MCP} and voltages from Table 4.1) giving rescaling factors 0.64 and 0.98 for C_{60}^{+} and C_{60}^{2+}, respectively. The rescaling factor for the higher charged ions is 1.00.

The acquisition of mass spectra is done using either a fast multiscaler card (P7886, FAST ComTec GmbH) or an analogue analyser card (AP240, Acqiris SA). The detector output is always connected with inputs of the data acquisition cards through an amplifier to decouple the cards from the detector and protect the expensive devices against possible electronic damages. For the detection of ions the amplifier with an amplification factor of 5 (model 352c, Novelec) is utilised, while the electron detection is done with an amplification of 10 (wideband amplifier

model 6954, Phillips Scientific).

The multiscaler P7886 card is based on a multistop time-to-digital converter (TDC) [PJB80, FST85]. Stop event pulses are generated by particles arriving at the detector. Such devices simply count and store time intervals between a start event and stop events. Then these data are converted into a histogram showing the number of events as a function of discrete time intervals (bins). The maximal resolution or time bin width is 500 ps. There is no dead time between time bins. The card is capable of counting only one event in every time bin. For all experiments presented here time bins are grouped by 32 and, hence, the card is used with the resolution of 16 ns. The start event is generated by a fast photodiode installed in front of the entrance window of the vacuum chamber. Each arriving ion produces a NIM peak through the discriminator (model 7011, FAST ComTec GmbH) which is used as a stop event. The major advantage of this counting method is the possibility to suppress the noise arising from the background ions and from the electronics by a proper setting of the discriminator level [SIm99]. This is especially important in the case of extremely weak signals. To determine the proper discriminator level the pulse height distribution (PHD) for the signal in front of the discriminator must be measured. Fig. 4.6 shows PHD for the different charged states of C_{60} ions obtained with the usual voltage settings: $U_{MCP} = -2.2$ kV, $U_{AC} = -2.0$ kV and the following laser parameters: $I = 5.2 \times 10^{13}$ W/cm^2, $\tau = 27$ fs, and $\lambda = 797$ nm. The very strong signals below 0.04 V correspond to noise. The signals above 0.04 V are due to the detection of C_{60} ions. They have asymmetric shapes with maxima in the range of $0.25 - 0.35$ V. The maximum of the peak distributions shifts to higher values with increasing C_{60} ion charge. This illustrates the fact that the ion kinetic energy after acceleration by the same voltage is larger for the higher ionised ions. Each signal curve has a local minimum (valley) around 0.04 V. Fortunately, the position of valley does not depend on the ion charge state and the trigger level can be set to 0.04 V in order to cut off the noise pulses below this value and to count C_{60} ionisation events independently of the ion charge state. Furthermore, the PHD contains important information about the relative detection efficiency of different ions [FHa02].

In the case of high ion yields detection methods based on the counting technique fail due to the possibility of two or more ions arriving within the same time interval (bin). In such situation it is better to employ analogue signal detection. The AP240 card is based on an analogue-to-digital converter (ADC) and allows one to digitise signal with 8-bit amplitude

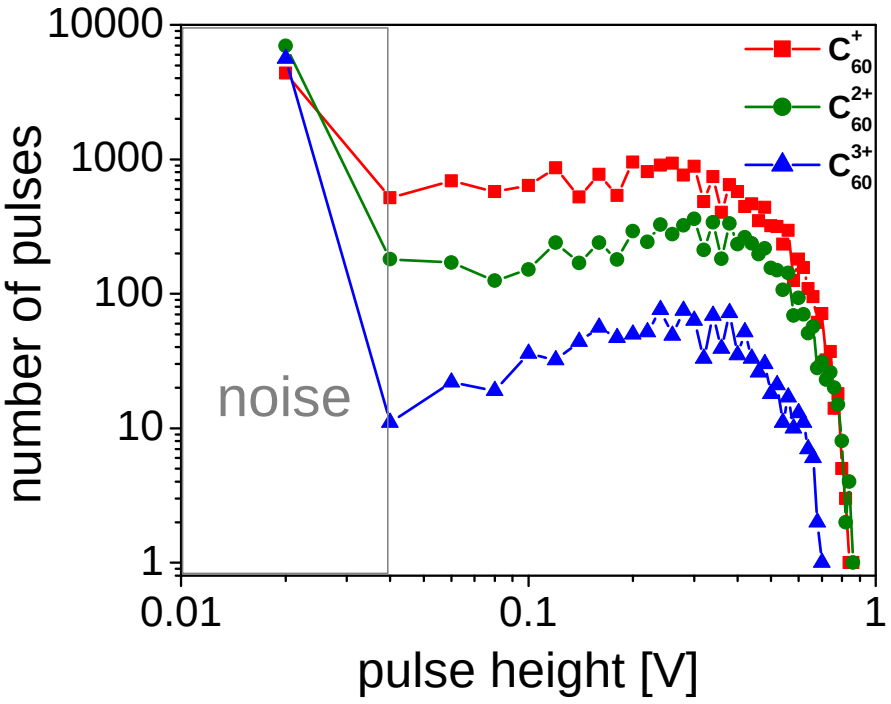

Figure 4.6: The distribution of pulse height for the different charged state of fullerenes.

resolution in real time at a maximal sampling frequency up to 2 GHz and then average it for up to 65536 laser shots [Rub05]. In addition to the simple averaging mode this card can be used for more complicated data acquisition procedures. In order to avoid overflow in the summed data, a fixed noise base can be subtracted from each signal value before the summation is done. Furthermore, there is an ability to set a threshold level and to detect only signals above this threshold. With the threshold the signals can be detected in counting or summation modes. In the counting mode the card counts events corresponding to the appearance of the signal above the threshold. In this mode the card runs as a counter possessing all advantages of the counting techniques. In the summation mode the card accumulates digitalised amplitudes of the signal if the signals are above the threshold level. This mode is especially interesting because of the possibility to combine advantages both the counting techniques and the techniques based on the analogue-to-digital converting. The noise can be minimised by the proper settings of the threshold, at the same time digitalisation of the incoming signal amplitude can overcome

the problem when more than one ion is detected in the same time bin. But these additional modes are not used in the present work and the card is only utilised for signal averaging because the averaging mode is most simple in operation and best suitable among others for quick measurements.

It is important to inspect stability and reproducibility of the mass spectra acquired. For that one can repeat the measurements of mass spectra many times and then calculate the standard deviation of the integrated ion yield for particular ions. Since the laser system stability influences the reproducibility of the mass spectra a test was performed with the laser used mostly in the present experiments. The outcome of such an examination for C_{60}^{+}, C_{60}^{2+}, and C_{60}^{3+} is shown in Fig. 4.7. The standard deviation in each point is computed using 100 separate mass spectra measured under identical conditions. Between 100 and 50000 laser shots were used for data accumulation to produce an individual mass spectrum and to obtain results plotted in Fig. 4.7. The standard deviation drops sharply down with an increasing number of a laser shots. Mass spectra obtained with more than 1000 laser shots demonstrate good reproducibility (the standard deviation $< 5\%$) and can be used for further data evaluation. Usually, individual mass spectra were acquired by averaging over 50000 laser shots. In pump-probe and polarisation dependent studies mass spectra were obtained by the averaging typically over $5000 - 10000$ laser shots. The mass spectra in the pulse shaping experiments were obtained by the averaging over $3000 - 5000$ laser shots.

The measured TOF mass spectrum $s(t)$ can be transformed into the mass spectrum depending on the mass-to-charge ratio $s\left(\frac{m}{q}\right)$ as

$$s\left(\frac{m}{q}\right) = s\left(A[t - t_0]^2\right) \quad , \tag{4.15}$$

where t is the measured ion arrival time, m/q is its mass-to-charge ratio, t_0 is the time delay between the ionisation event in the vacuum chamber and the electronics triggering time, and A is a scaling factor. A and t_0 can be determined from the mass-to-charge ratios m_1/q_1 and m_2/q_2 of two specific, well known ion peaks in the TOF mass spectrum which have the arrival times t_1 and t_2

$$A = \left(\frac{\sqrt{\frac{m_1}{q_1}} - \sqrt{\frac{m_2}{q_2}}}{t_1 - t_2}\right)^2 \tag{4.16}$$

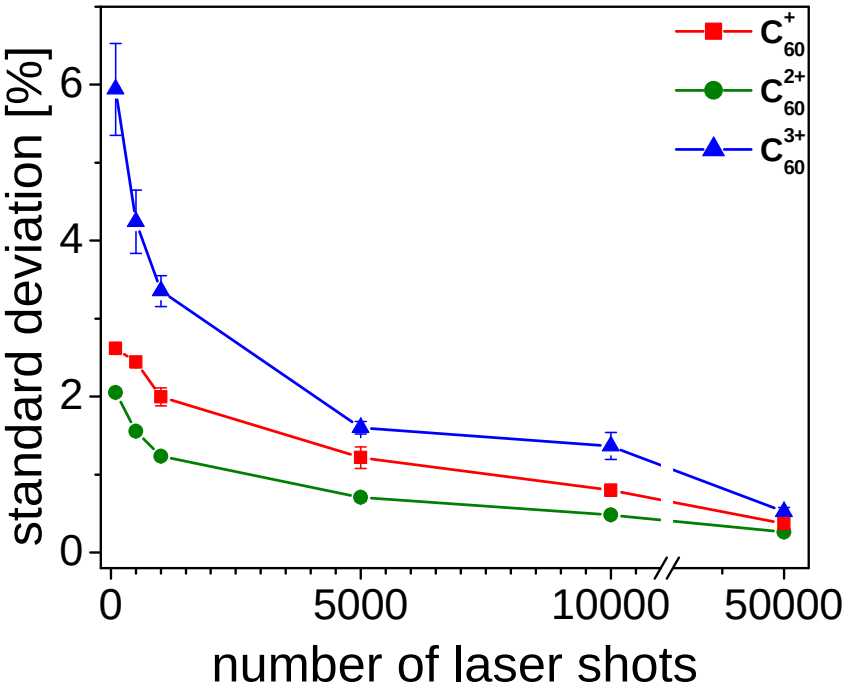

Figure 4.7: Dependence of the standard deviation of the integrated ion yield on the number of laser shots used for the acquisition.

and

$$t_0 = \frac{\sqrt{\frac{m_1}{q_1}/\frac{m_2}{q_2}}t_2 - t_1}{\sqrt{\frac{m_1}{q_1}/\frac{m_2}{q_2}} - 1} \quad . \tag{4.17}$$

Normally, mass spectra of C_{60} fullerenes are calibrated by the arrival times of C_{60}^{+} and C_{60}^{3+} ions. The conformation of peak assignment can be done by the inspection of different peaks positions in the mass spectrum (for example, C_{60}^{2+} or/and Xe^{+}). To keep the integrated ion yield per mass-to-charge interval $s\left(\frac{m}{q}\right)\Delta\left(\frac{m}{q}\right)$ equal to the integrated ion yield per time interval $s\,(t)\,\Delta t$, the mass spectrum has to be recalculated taking into account the following Jacobian

$$s\left(\frac{m}{q}\right)\Delta\left(\frac{m}{q}\right) \propto t\, s(t)\Delta t \quad . \tag{4.18}$$

One example of a TOF mass spectrum for C_{60} fullerenes obtained with the laser parameters $I = 1.4 \times 10^{14}\,\mathrm{W/cm^2}$, $\tau = 27\,\mathrm{fs}$, and $\lambda = 797\,\mathrm{nm}$ is presented in Fig. 4.8a. Exactly the

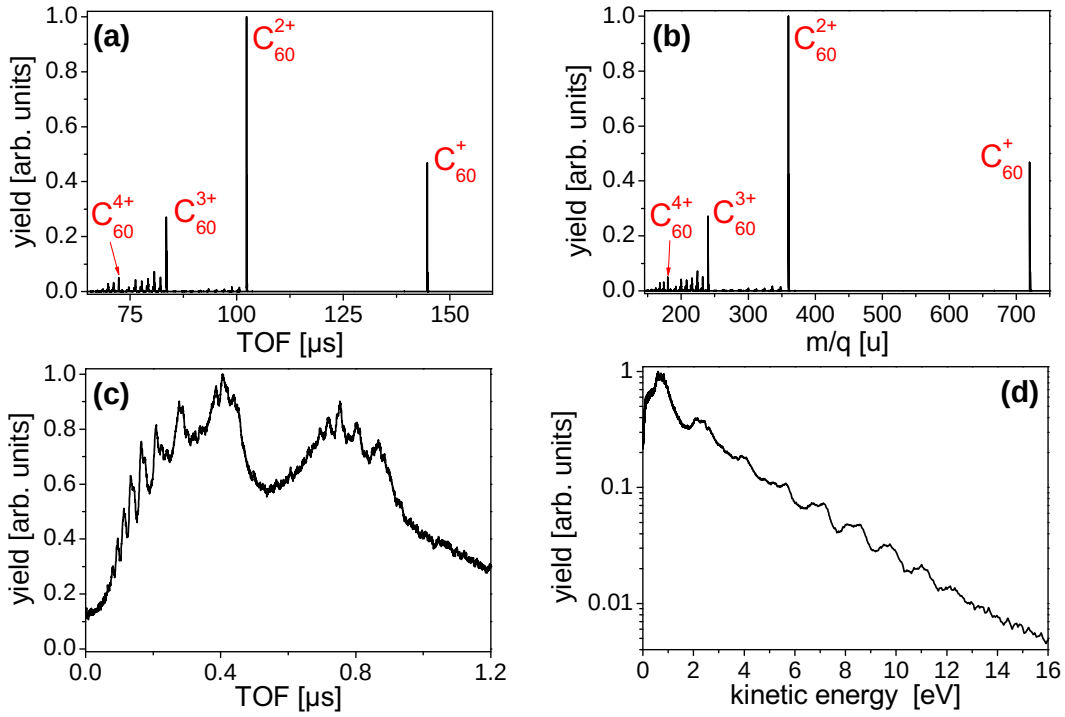

Figure 4.8: (a) TOF mass spectrum of C_{60} fullerene; (b) the same spectrum as Fig. 4.8a but plotted as a function of m/q; (c) photoelectron spectrum of C_{60} fullerene; (d) the same spectrum as Fig. 4.8c but modified accordingly to Eq. (4.22) and plotted on the logarithmic scale as a function of E_K. In all cases the laser parameters are: $I = 1.4 \times 10^{14}\ W/cm^2$, $\tau = 27\ fs$, and $\lambda = 797\ nm$.

same mass spectrum but plotted on m/q scale (without Jacobian transformation) is shown in Fig. 4.8b.

The photoelectron detection scheme is very similar to one operated for the ions detection. This scheme is depicted in Fig. 4.5b. The main difference is the absence of any extra voltage between the grounded grid and the MCP front surface. Only the bias voltage $U_{MCP} = 2.5\,\text{keV}$ is applied. Such settings correspond to voltage of $1135\,\text{V}$ per MCP plate. It is slightly more than voltage recommended by the specification ($1100\,\text{V}$) but with lower MCP voltage a good signal to noise ratio in photoelectron spectra can not be achieved.

Photoelectron spectra are acquired with $0.5\,\text{ns}$ temporal resolution using AP240 analyser platform connected to the MCP detector output through the wideband amplifier model 6954 with an amplification factor of 10.

The transformation of the measured TOF photoelectron spectrum $s(t)$ into the photoelectron spectrum depending on the kinetic energy of photoelectrons $s(E_K)$ can be written as

$$s(E_K) = s\left(A\frac{1}{[t-t_0]^2}\right) \quad , \tag{4.19}$$

where t is the measured TOF of a photoelectron, E_K is its kinetic energy, t_0 is the time delay between the ionisation event in the vacuum chamber and the electronics triggering time, and A is a scaling factor. One way of determination of A and t_0 for photoelectron spectra is more complex than for mass spectra. For that one has to make an assumption about kinetic energies E_{K1} and E_{K2} for at least two peaks in the TOF photoelectron spectrum with flight times t_1 and t_2. It can be fulfilled by either the kinetic energy assignment of Rydberg peaks in C_{60} photoelectron spectra [BLH05] or the resonance structure inspection of ATI peaks in photoelectron spectra of xenon measured at several well known laser intensities [SLH98]. If this is done, A and t_0 can be determined with the following expressions

$$A = \left(\frac{t_2 - t_1}{\sqrt{\frac{E_{K1}}{E_{K2}}} - 1}\right)^2 E_{K1} \tag{4.20}$$

and

$$t_0 = \frac{t_1\sqrt{\frac{E_{K1}}{E_{K2}}} - t_2}{\sqrt{\frac{E_{K1}}{E_{K2}}} - 1} \quad . \tag{4.21}$$

The energy resolution of the photoelectron spectrometer within the range of interest ($0.5 - 20\,\text{eV}$) varies with E_K from $1\,\text{meV}$ at $E_K = 0.5\,\text{eV}$ to $92\,\text{meV}$ at $E_K = 20\,\text{eV}$.

The integrated photoelectron yield per time interval Δt is $s(t)\Delta t$ and per kinetic energy interval ΔE_K is $s(E_K)\Delta E_K$. The time interval Δt in any TOF photoelectron spectrum is a constant. At the same time, after the transformation of the TOF photoelectron spectrum $s(t)$ into the photoelectron spectrum depending on the kinetic energy of photoelectrons $s(E_K)$ according to Eq. (4.19), the kinetic energy interval ΔE_K depends on E_K. Hence, to keep the integrated photoelectron yield per kinetic energy interval identical with the integrated photoelectron yield per time interval for the whole range of E_K, the photoelectron spectrum can be recalculated with the following formulas

$$s(E_K)\Delta E_K \propto t^{-3} s(t)\Delta t \tag{4.22}$$

or

$$s(E_K)\Delta E_K \propto E_K^{3/2} s(t)\Delta t \quad . \tag{4.23}$$

This modification can by done by the applying either Eq. (4.22) before the TOF scale transformation or Eq. (4.23) after the transformation. Fig. 4.8c-d show the TOF photoelectron spectrum of C_{60} fullerenes and the photoelectron spectrum depending on E_K, respectively. The laser parameters are identical to the parameters used for the measurements of the mass spectrum presented in Fig. 4.8a-b. The intensity of the photoelectron spectrum depicted in Fig. 4.8d is modified accordingly to Eq. (4.22) and plotted on the logarithmic scale.

Both the multiscaler P7886 card and the AP240 analyser platform are capable to be run with LabVIEW software. It allows one to automate the acquisition of mass or photoelectron spectra in the experiments requiring many repetitions of spectral measurements, as needed for laser intensity or/and polarisation dependent studies, optimisations with a pulse shaper, and pump-probe experiments.